RSC Advances

ROYAL SOCIETY OF CHEMISTRY

PAPER

View Article Online
View Journal | View Issue

Cite this: *RSC Adv.*, 2021, **11**, 28621

Ultrahigh compressibility and superior elasticity carbon framework derived from shaddock peel for high-performance pressure sensing†

Na Zheng,[ab] Changzhou Chen, *[ab] Mengqi Tang,[ab] Weixin Wu,[ab] Yan Jiang[ab] and Douyong Min[ab]

Shaddock peel, a crop by-product mainly composed of cellulose, hemicellulose, lignin, and pectin, was developed as a flexible sensitive material for detecting environmental external pressure. Firstly, a natural carbon framework (C-SPF) with high conductivity was prepared using hydrothermal treatment followed by carbonization. Then, the PDMS elastomer was coated on the C-SPF instead of dense filling to convert the brittle C-SPF into elastic porous materials (M-SPF). Benefiting from the large deformation space of the porous framework and the stable interactions between PDMS and C-SPF, M-SPF exhibited ultrahigh coercibility (up to 99.0% strain) and high elasticity (99.4% height retention for 10 000 cycles at 50.0% strain). The M-SPF-based pressure sensor also exhibited a quick response (loading and unloading times were 20 ms and 30 ms), high sensitivity (63.4 kPa^{-1}), wide working range (from 0 to 800 kPa), and stable stress-electric current response (10 000 cycles). These advantages open a door to a variety of applications, such as flexible wearable devices, which demonstrated human physiological signal monitoring. The low cost, simple design and portable use of piezoresistive sensors highlight the potential application of the crop by-product shaddock peel as a high-value material.

Received 16th April 2021
Accepted 15th August 2021

DOI: 10.1039/d1ra02978a

rsc.li/rsc-advances

1. Introduction

Flexible pressure sensors, which can convert external pressure into an electrical signal output have been extensively studied for many applications, such as smart wearable electronic devices,[1] electronic skins,[2] robots,[3] sports motion,[4] and health monitoring.[5] Different sensing mechanisms have been explored in developing various types of flexible pressure sensors, including piezoresistive,[6,7] piezoelectric,[8] capacitance,[9] and triboelectric[10] sensors. Piezoresistive sensors have a simple structure and their advantages are low cost and short response time. Until now, it has been a challenge to use impedance-type pressure sensors to monitor complex human physiological signals, including small body motion signals (such as pulses) and large deformation body motions (such as joint motion), as the sensors cannot simultaneously obtain high sensitivity, a wide working pressure range, and durability. Therefore, there is an urgent need to develop pressure sensor materials with high elasticity, excellent fatigue resistance, and current sensitivity stability.

Advanced conductive materials and robust constructions are two effective means of improving flexible pressure sensor sensitivity and working pressure range. Hence, nanomaterials, such as metal nanoparticles,[11] metal nanowires,[12] metal frameworks,[13] two-dimensional transition metal materials[14,15] carbon nanotubes (CNTs),[16] graphene,[17–19] and conductive polymers,[20–22] have been used as conductors in flexible piezoresistive pressure sensor fabrication. Additionally, easily deformable structures, such as 3D porous structures and micro-sized arrays, also improve conductive material and/or flexible substrate performance by increasing the variation in their electrical contacts under pressure loadings.[23] These reported pressure sensors have exhibited good performance. However, these sensors need high-cost raw materials and complex and expensive fabrication processes, as well as yielding environmentally hazardous production byproducts, which limit their widespread commercial uses. Besides, sensors based on metals, particularly metal nanowires and nanoparticles, are unstable due to their poor reproducibility and limited chemical stability. Therefore, piezoresistive flexible sensor preparation should use low cost, facile, environmentally friendly, and reproducible approaches.

As an alternative to fossil resources and metals, inexpensive and renewable biomass resources, such as wood,[24] cellulose,[25] lignin[26] and chitosan,[27] have emerged as ideal precursors of conductive carbon materials for pressure sensors. These biomass-based pressure-sensing materials have shown

[a]*Guangxi Key Laboratory of Clean Pulp and Papermaking and Pollution Control, Nanning, 530004, People's Republic of China. E-mail: chenchangzhou@gxu.edu.cn; Tel: +86-0771-3237305*

[b]*College of Light Industry and Food Engineering, Guangxi University, Nanning, 530004, People's Republic of China*

† Electronic supplementary information (ESI) available. See DOI: 10.1039/d1ra02978a

comparable performance with partial graphene-based and CNT-based pressure sensing materials, which implies the great potential for biomass-based pressure sensing material applications. However, the development of wood derived pressure sensors is challenging, requiring a long time chemical pretreatment, producing waste liquid and with there being different pressure responses of the different wood sections (transverse and longitudinal). Since the biomass carbon-based pressure sensor market is not yet a reality, much more effort should be made to further develop raw materials that are more reasonable and methods for enhancing their pressure sensing performance.

Shaddock as a cash crop is widely grown in southern China; the economic benefits of shaddock are mainly implemented by shaddock pulp in factories. However, a huge amount of shaddock peel is usually considered as by-product and discarded. Actually, the excellent performance of SP lies in its 3D lignocellulosic honeycomb structure, which is mainly composed of carbohydrates (cellulose, hemicellulose and pectin) and lignin.[28] Many studies have proved that Shaddock peel (SP) is a good precursor of porous carbon materials. Various applications of porous carbon materials derived from SPs have been extensively studied, including supercapacitors,[29] carbon-based materials,[30] and adsorbents.[31] These SP-based carbon materials generally need activation steps to destroy the 3D network framework, which is unconducive to preparing high-performance pressure sensing materials. As mentioned above, a pressure sensor with good performance requires highly conductive materials and a macro 3D porous framework. Hence, an SP-based 3D carbon network framework fabricated with high conductivity and high elasticity for high-performance pressure sensors is needed.

Here, we report a flexible, lightweight and highly conductive porous PDMS-modified SP-based carbon framework for piezoresistive pressure sensors with high performance *via* a facile method. After SP hydrothermal treatment, a brittle, highly conductive SP-based carbon framework (C-SPF) with multilevel porosity was obtained through carbonization. Then, the PDMS elastomer was coated on the C-SPF framework instead of dense filling to convert the brittle C-SPF into conductive porous elastic materials (M-SPF). Benefiting from the large deformation space of the porous framework and the stable interactions between PDMS and C-SPF, M-SPF exhibited super-compressibility and hyperelasticity, which resisted a supreme compressive strain of 99.0% and maintained 99.4% height reservation after 10 000 cycles at a strain of 50.0%. The as-prepared M-SPF-based piezoresistive sensor exhibited fast responses to loading and unloading stress of 20 ms and 30 ms, respectively. Furthermore, the sensor displayed a high sensitivity (63.4 kPa^{-1}), a wide working pressure range (from 0 to 800 kPa), and a stable stress-current response (10 000 cycles). We demonstrated the potential for a practical wearable device with an M-SPF-based pressure sensor by monitoring tiny movements of the human body, such as pulses, facial expression changes, and joint motion. This work not only provides a facile way to develop high performance pressure sensing materials for fabricating flexible wearable electronic devices, but also shows encouraging prospects in high-value and sustainable development of crops by-product.

2. Experimental section

2.1. Materials and reagents

Fresh shaddocks were purchased from a local market in Guangxi. Analytical grade *n*-hexane ($CH_3(CH_2)_4CH_3$) and polydimethyl siloxane (PDMS) were purchased from Aladdin. Conductive silver paste (3701) was purchased from Luode reagent company.

2.2. Shaddock peel carbon framework preparation

Fresh shaddocks were peeled, and the shaddock peels (SP) were cut into pieces of 4 cm × 2.5 cm × 2.5 cm in size and washed with distilled water. Then, the SP was soaked in 70 mL distilled water in a Teflon-lined autoclave and heated at 180 °C for 10 h. When the autoclave cooled down, washed the treated SP for several times with deionized water and then freeze-dried for 2 days at −50 °C to obtain the hydrothermal shaddock peel framework (H-SPF). The obtained H-SPF was carbonized at 800 °C for 2 h in the atmosphere of Ar gas to obtain a carbonized shaddock peel framework (C-SPF).

2.3. Pressure sensing material preparation

The flexible pressure sensing material is manufactured by a simple blending method. Firstly, PDMS was prepared by mixing 1.0 g base agent and 0.1 g curing agent, and then diluted with 10 mL *N*-hexane (the optimization condition can be found in ESI†). Next, C-SPF (size is 20 mm × 10 mm × 10 mm) was immersed in the above mixed solvent and stand still for 10 min to ensure the C-SPF pores full-fill infiltrated with PDMS completely. The soaked C-SPF was removed and placed into a vacuum environment (approximately −0.09 MPa) at room temperature (25 °C) for 2 h to remove the *N*-hexane and obtain uncured PDMS-coated C-SPF. Finally, the uncured PDMS-coated C-SPF was cured at 80 °C for 8 h to obtain the flexible shaddock peel-based carbon material, which was named M-SPF.

2.4. Fabrication of the M-SPF based pressure sensors

M-SPF was cut into certain length (10 mm), width (10 mm) and thickness (2 mm). Then, two pieces of polyethylene terephthalate (PET) with regular rectangle was prepared and washed with deionized water. After that conductive silver paste was smeared on the surface of the M-SPF to eliminate the contact resistance of the flexible sensor. Two copper tapes were stuck to the opposite sides of the sensor. At last, PET was utilized to encapsulate M-SPF to avoid the environment influence. The M-SPF based pressure sensor finally presented a sandwiched structure (Fig. S1†).

2.5. Characterizations

The microstructures of the materials were observed by scanning electron microscopy (SEM; SU8220, Hitachi) equipped with EDS energy spectrometer Resistivity was measured using a high-precision resistance test instrument (YAOS, FM100GH). X-ray diffraction (XRD) patterns were recorded by a SmartLab3k diffractometer. Raman spectrometer was carried out on

a confocal laser micro Raman spectrometer (LabRAM HR Evolution, HORIBA Jobin Yvon) at 532 nm laser. Thermogravimetric analysis was conducted on a thermogravimetric analyzer (TG, Diamond TG/DTA6300, PerkinElmer. 8A). FT-IR analysis was recorded using an FT-IR Microscope (Thermo Nicolet Corporation, Madison). The specific area was calculated by Brunauer–Emmett–Teller (BET) method and Barrett–Joyner–Halenda (BJH) method by Micromeritics ASAP 2460. The micro-active AutoPore V 9600 mercury intrusion manometry (MIP) was used to measure porosity and macropore size distribution. Mechanical properties were evaluated by universal material machines (Instron 3367A, England) with a 2 kN load cell. The electrical signal was recorded by using an electrochemical workstation (CHI660E) under 1.0 V applied voltage.

3. Results and discussion

3.1. Fabrication and characterization of the materials

The elastic shaddock peel carbon fabrication steps were illustrated in Fig. 1a. The fresh SP had a 3D honeycomb-like porous structure with a pore size of approximately 120 μm (Fig. 1b and j) and porosity of 89.0% (Table S1†). Compared with direct carbonization, hydrothermal carbonization (HTC) was conducive to maintaining a complete 3D porous framework during the subsequent carbonization process. Therefore, the SP was hydrothermally pretreated to obtain H-SPF. After HTC, the treated SP was brown and displayed a smaller pore size mainly at approximately 100 μm (Fig. 1c and k) and a larger porosity of 94% (Table S1†). This may due to that partial carbohydrates of the SP pore wall were carbonized or removed during the HTC process.[32] High skeleton conductivity was needed to achieve a stable detectable electrical current through the composite.[33] Therefore, a subsequent high-temperature carbonization treatment was applied to convert H-SPF into a conductive 3D carbon framework.

The TG curve of H-SPF (Fig. S2†) showed that the H-SPF mass reduction rate gradually slowed above 600 °C. To identify the optimal carbonization conditions, the temperature was increased from 600 to 900 °C, and the resistivity of the obtained C-SPF samples was also tested. The resistivity test results (Fig. S3†) showed that the C-SPF samples sharply declined when the carbonization temperature rose from 600 °C to 700 °C and

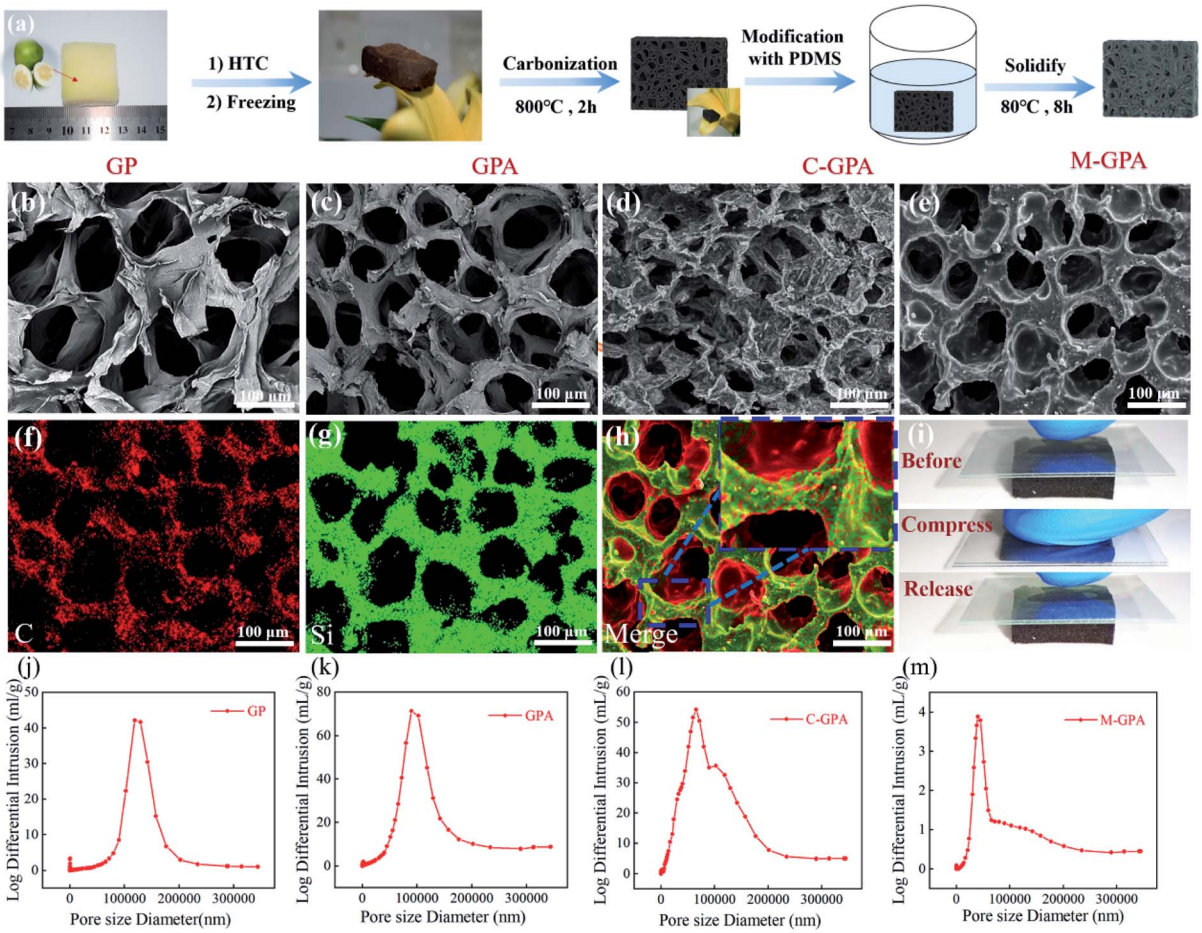

Fig. 1 (a) Scheme for the process of preparing M-SPF. SEM images of (b) SP, (c) H-SPF, (d) C-SPF and (e) M-SPF. EDS mapping results. Individual mapping result of carbon (f) and silicon (g) elements of M-SPF sample surface. (h) Mixed mapping result of silicon (green) and carbon (red) elements. (i) Real-time digital images of an M-SPF sample during the compressive and recovery process. The pore size distribution of (j) SP, (k) H-SPF, (l) C-SPF and (m) M-SPF calculated by mercury intrusion porosimetry (MIP) method.

then slightly decreased with a further increase in temperature. For the sake of saving energy, the carbonization temperature was set at 800 °C. The Raman spectra of C-SPF (Fig. S4†) obtained at 800 °C showed that the intensity ratio between the D peak (1348 cm^{-1}) and G peak (1580 cm^{-1}) was 0.68, which indicated good crystallinity and high C-SPF conductivity (38.2 s m^{-1}). The SEM image (Fig. 1d) showed that C-SPF had a connected three-dimensional framework with multileveled pores (the micro-pore size was approximately 70 μm) and a high porosity of 93.0% (Table S1†), which was confirmed by MIP (Fig. 1i). Moreover, the porous C-SPF wall was wrinkled and exhibited a gully structure compared with H-SPF. Such a cellular structure in the 3D framework and wrinkled gully structure in the porous wall provided a high specific surface area of 625 m^2 g^{-1} (Fig. S5†), which ensured modifier accessibility to the absorptive surface. The unmodified C-SPF showed significant stiffness and brittleness and easily collapsed even at a small compression stress (Fig. S6†). To endow C-SPF with better flexibility, elasticity, and stability, the typical polydimethylsiloxane (PDMS) elastomer was coated into the 3D carbon framework through immersing, vacuuming, and curing process. SEM (Fig. 1e) and EDS (Fig. 1f–h) images showed that PDMS was uniformly coated on the C-SPF hole wall. Furthermore, there is still some carbon contact sites exposed on the surface of the material which could allow the electrical contact between the electrodes and the material surface. At same time, the obtained M-SPF maintained a good 3D porous framework with a rough, porous surface. Owing to PDMS infiltration, the M-SPF pores were clearly revealed and became relatively smaller, mainly at approximately 50 μm (Fig. 1m). Interestingly, the modified C-SPF had a porosity of 65.0% (Table S1†) and could be easily compressed with the desired deformations (Fig. 1i). Otherwise, the conductivity test showed that the prepared M-SPF had good electrical conductivity with 1.47 s m^{-1}. These M-SPF characteristics make it suitable for preparing high-performance pressure sensors. Additional detailed mechanical and electrical properties are discussed below.

The surface chemistry changes during fabrication were also investigated. The XPS spectra are shown in Fig. 2a, and the C/O ratios are illustrated in Table S1.† The SP, H-SPF and C-SPF C/O ratios were calculated as 2.10, 2.53, and 9.59, respectively. This indicated that only mild SP carbonization occurred during HTC treatment, while the degree of carbonization further increased drastically when H-SPF was applied in the carbonization pyrolysis process. The sudden decrease in the M-SPF C/O ratio of 1.19 resulted from the PDMS coat O atoms. Otherwise, compared with SP, H-SPF and C-SPF, the FT-IR spectrum (Fig. 2b) of M-SPF showed strong characteristic PDMS peaks at 1259 cm^{-1} (Si-CH_3),[34] 1209, and 1072 cm^{-1} (Si–O–Si).[35] From Si 2s (152) and Si 2p (101) peaks were observed in M-SPF.[36] Compared with the XRD results of SP (Fig. 2c), the disappearance of the peak at 15.8° and the widening of the peak at 22.0° in the C-SPF spectrum compared with SP and H-SPF suggested cellulose crystallization zone destruction and amorphous carbon formation during the high-temperature carbonization process. The new peak at 12.4° corresponding to the PDMS microcrystal diffraction in the M-SPF spectrum suggested successful PDMS introduction into the C-SPF framework. The M-SPF (*020*) diffraction peak at 22.0° had no obvious change compared with C-SPF, indicating the non-covalent reaction between PDMS and C-SPF during the modification process.

3.2. The mechanical performances of M-SPF

The penetrated PDMS molecules provided robustness and flexibility by interconnecting the surrounding C-SPF pore wall, creating an elastic M-SPF 3D framework. As shown in Fig. 3a and c, the M-SPF stress–strain plots at 50% strain in the 100th, 1000th, and 10 000th cycles were almost uniform with the first cycle. Besides, extremely high stress retention (97.4%) and height retention (99.4%) were obtained after 10 000 cycles, which were higher than other biomass-based and 3D carbon materials (Fig. 3e).[57–65] Moreover, even under harsh compression conditions (90.0% strain for 1000 cycles), M-SPF still retained over 80% of its maximum stress and shows only a 1.7% reduction in height. These results illustrated that M-SPF could tolerate large elastic deformation without accumulating damage or undergoing structural collapse.[37] The energy loss coefficient was approximately 35.0–29.0% from the first to 10 000th cycles at 50% strain (Fig. 3b) and 33.0–27.0% from the first to 1000th cycles at 90.0% strain (Fig. 3d). These observations indicated relatively lower energy dissipation than that of other pressure sensing materials (Fig. 3f),[66–72] suggesting M-SPF's preeminent energy absorption competence profiting from the effective stress transfer among the pore wall carbon layers.[38,39] As

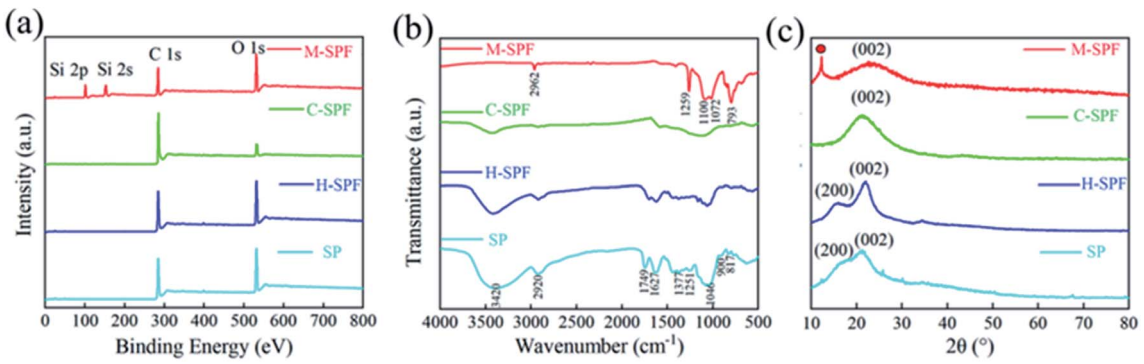

Fig. 2 (a) XPS spectra, (b) FT-IR spectra, and (c) XRD of the samples.

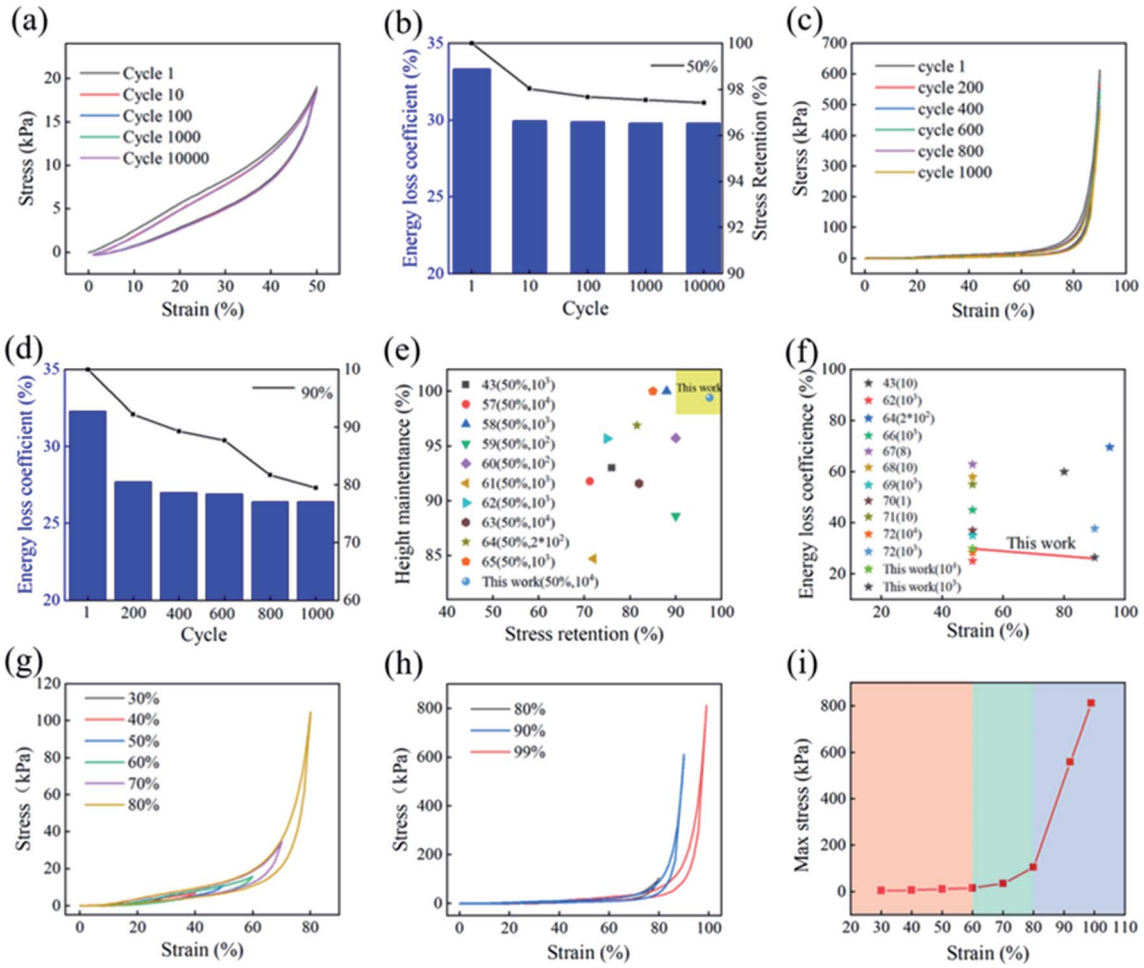

Fig. 3 (a) M-SPF continuous 10 000 cyclic loading–unloading curves under 50% compression strain. (b) M-SPF energy loss coefficient during 10 000 consecutive cycles. (c) Stress–strain curves at 90% strain for 1000 cycles. (d) M-SPF energy loss coefficients in cyclic compression tests (80% strain). (e) and (f) Comparison of height retention, stress retention and energy loss coefficients for various compressible materials. (g) and (h) M-SPF compression loading–unloading tests at different strains. (i) M-SPF maximum stress at different strains.

shown in Fig. 3g and h, M-SPF had good mechanical response signals for different compression strains. The stress remained above zero and could return to the starting point during the unloading process, indicating complete elastic recovery without plastic deformation.[40] The loading curve from 0 to 99.0% strain (Fig. 3i) exhibited three representative regions, involving the elastic region, yield region, and densification region, which consistent with CNT-based and graphene-based frameworks.[16,41] The first linear region (strain 0–60.0%) was broader than previously reported frameworks,[42,43] suggesting excellent pore wall elastic bending as a result of the stable interactions between PDMS and the C-SPF framework. In the second yield region (60.0–80.0%), the part of pores was crushed and partially irreversibly damaged; thus, this region was short and followed by an inflection point. With

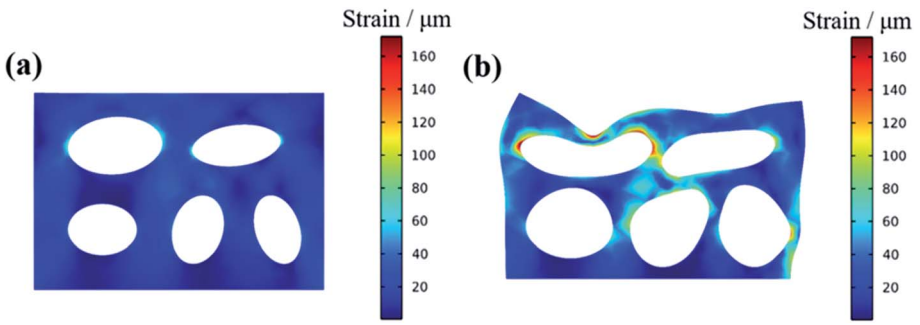

Fig. 4 Finite element analysis of (a) M-SPF and (b) C-SPF under a certain external force.

increasing compressive stress (80.0–99.0%) in the densification region, the pore walls were set about colliding with each other.

In order to verify the influence of the PDMS on the mechanical properties of C-SPF, finite element analysis method (COMSOL Multi-physics) was conducted to simulate the deformation of the materials with and without PDMS under a certain pressure.[44] The properties of each material for the simulation work were listed in Table S2.† For the M-SPF models, the thickness of PDMS layer on the C-SPF was set to be around 10 μm. The size of both C-SPF and M-SPF models were set to be the same length (300 μm), width (200 μm) and height (50 μm) for the purpose of comparison. In the simulation process, the bottom surface of the simulated material was fixed and an external force of 10 Pa was applied to the top surface. As shown in Fig. 4, C-SPF shows high deformation under an external force while the PDMS-modified C-SPF has no obvious deformation, indicating that the coating of PDMS can greatly improve the compressive strength of the carbon skeleton of C-SPF.

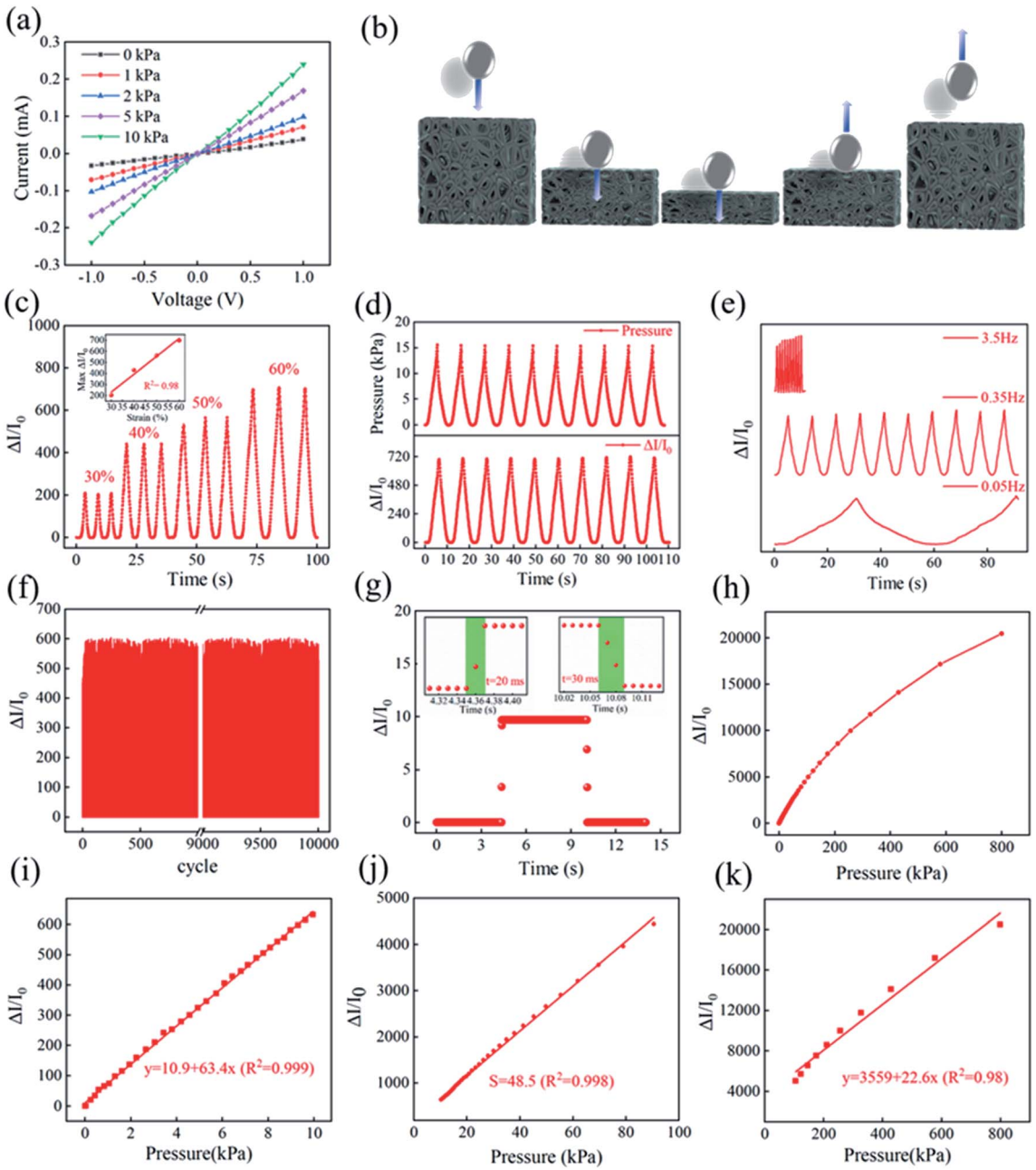

Fig. 5 (a) M-SPF current–voltage properties under different pressures. (b) The model to simulate the compression process. (c) The current responsivity at different strains. The inset shows the current as a function of strain with a good linear relationship ($R^2 = 0.98$). (d) M-SPF response at different compression frequencies. (e) M-SPF-based sensor durability test at 50% strain for 10 000 cycles. (f) M-SPF response after 10 000 compressed-released cycles. (g) Sensor step response to constant pressure. The inset shows magnified response times at pressure loading (left) and unloading (right). (i–k) Sensitivity over a wide range of pressures.

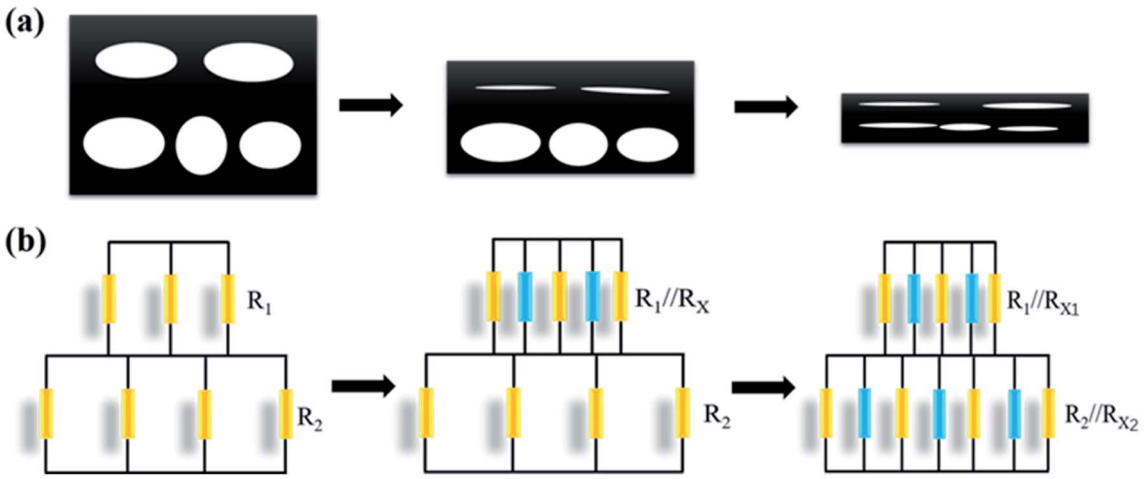

Fig. 6 M-SPF structure model (a) during compression (b) and equivalent circuit model.

3.3. Pressure sensing properties of M-SPF

Based on its mechanical stability, good conductivity, large compression strain and excellent durability, M-SPF is a promising candidate for piezoresistive sensors. The M-SPF based pressure sensor electro-performance was tested in the loading pressure ranging from 0 to 800 kPa, and the electrical signals were monitored by an electrochemical workstation. As shown in Fig. 5a, the current–voltage (*I*–*V*) curves of M-SPF pressure sensor exhibited typical ohmic characteristic under a fixed pressure, suggesting that the contact resistance is regardless,[45] which could be attributed to the exposure of carbon contact sites and the use of conductive silver paste. In addition, a brightness change of a light-emitting diode (LED) lamp in the integrated circuitry indicated the M-SPF sensor resistance change (Fig. S7†). The white LED light was dim without pressure and bright under applied pressure. This could be explained using a ball pressure model (Fig. 5b). When the M-SPF was compressed under external force by falling glass balls, the framework pore size shrank, and the distance between adjacent conductive hole walls decreased. Both shorter conductive paths improved the conductivity of the prepared sensor.[46] This reduced the compressed M-SPF resistance in the circuit, which caused the LED lamp to become brighter. When the glass ball bounced, the M-SPF aperture size and the distance between the hole walls began to return to the original state, and the M-SPF resistance increased. This view was also verified by the SEM images (Fig. S8†) of M-SPF in compressed and released states.

Based on the results of above mechanical performance test and finite element analysis, we established an equivalent circuit model to explain the conduction mechanism followed a previous study.[47] As seen in the Fig. 6, the skeleton of M-SPF was regarded as a resistor network. The resistance of the composite material (R) could be expressed as:

$$R = R_1 + R_2 \quad (1)$$

where R_1 and R_2 represent the resistance of the upper layer and the lower layer of the network, respectively.

When the strain was small, the apertures of upper layer were flattened first, and the corresponding conductive connections were formed. The resistors of upper layer consisted of initial resistor R_1 and the added resistor R_x of new conductive pathways in parallel. However, the R_2 was unchanged since the aperture of lower layer only deformed without new form of conductive connections. Therefore, the total resistance was equivalent to:

$$R = R_1//R_{x1} + R_2 \quad (2)$$

where R_{x1} represents the resistance of new conductive pathways.

When the deformation was increased, the apertures of the lower layer were compressed and a large amount of conductive connections would be formed. The total resistance was equivalent to:

$$R = R_1//R_{x1} + R_2//R_{x2} \quad (3)$$

where R_{x2} represents the resistance of new conductive pathways.

The prepared pressure sensor performance was further investigated. Using the measured current, the prepared M-SPF sensor response was calculated by the relative current change (RCR, $\Delta I/I_0 = (I_P - I_0)/I_0$, where I_P and I_0 were the current with and without applied pressure, respectively). As shown in Fig. 5c, the response signal intensity correlated well to the pressure input, which was indicated pressure load. The prepared sensor output curve demonstrated excellent linearity ($R^2 = 98.0\%$) in the strain region up to 60.0% (the inset in Fig. 5c), suggesting that the M-SPF sensor could greatly simplify the signal process in practical applications involving a large dynamic range of pressures. Furthermore, RCR could be used to monitor the prepared sensor's external pressure change. As shown in Fig. 5d and e, the RCR real-time curve was synchronous with the stress signal, and the response signal frequency was consistent with the corresponding input pressure frequency (from 0.05 to 3.5 Hz) without obvious delay. These results indicated that the prepared M-SPF sensor had an immediate response to the applied pressure. As shown in Fig. 5f and S9,† the cycle test of

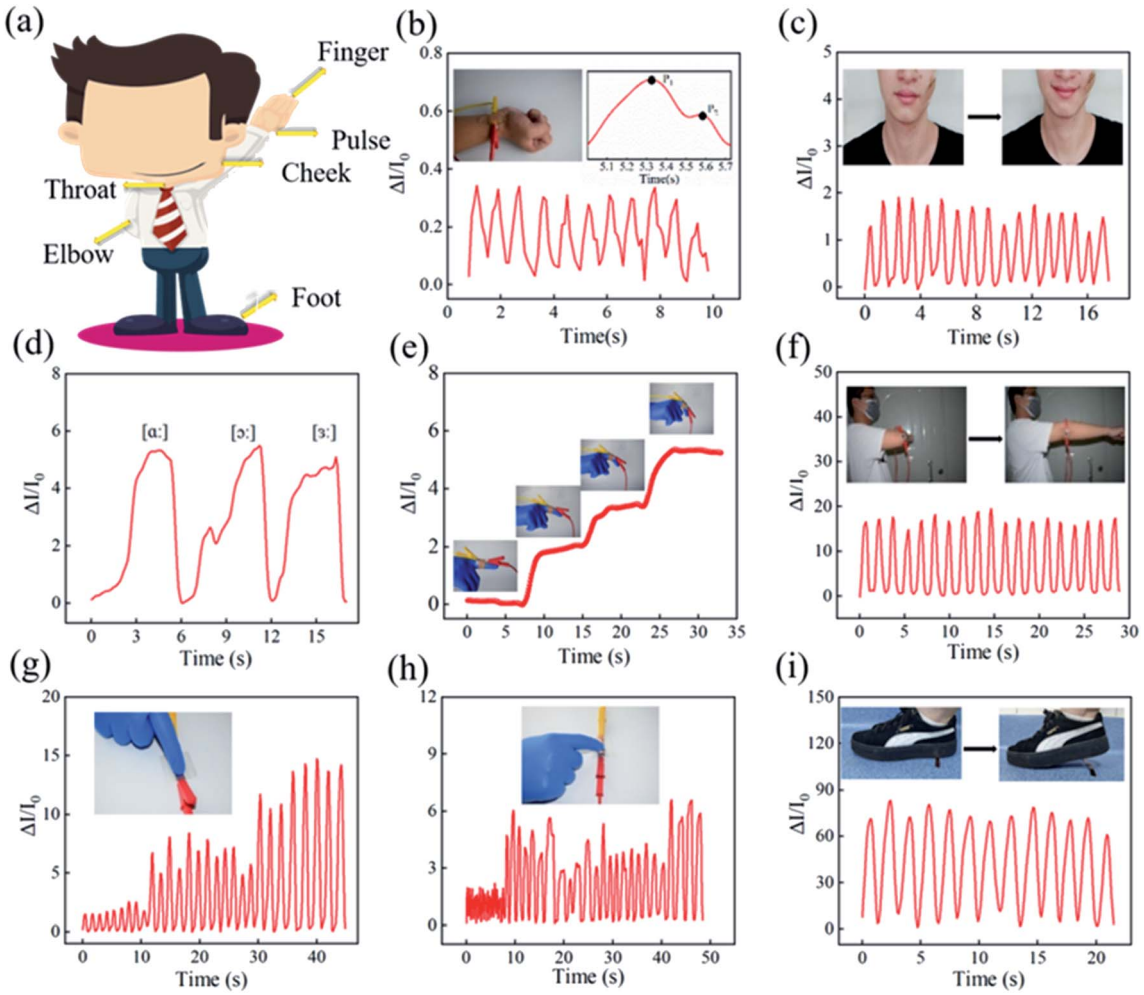

Fig. 7 (a) Different detection regions of the human body. (b) Pulse detection. Real-time current response of the fabricated sensor to (c) cheek when smiling and (d) throat when saying different phonetic symbols (/ɑ://ɔ://ɜ:/). Motion detection of (e) fingers and (f) bended elbow. Real-time current response of the fabricated sensor to finger compressions with different (g) intensities and (h) frequencies. (i) Foot movement detection.

M-SPF exhibited a highly reproducible pressure response after 10 000 cycles at 0.35 Hz under 50.0% strain, which was comparable to the reported CNT and GO based pressure sensors in previous studies.[48,49] This not only indicated the strong fatigue resistance of the sensing material, but also the well contact between the sensing material and the electrode. The magnified output curve turning points in Fig. 5g shows that the M-SPF response times were 20 ms and 30 ms for pressure loading and unloading, respectively. This fast response illustrated the practicability of pressure load detection, such as for robotic and medical applications.

Sensitivity is another important sensor performance parameter. The pressure sensitivity, S, was defined as the slope of the RCR-compression stress curve ($S = \delta(\Delta I/I_0)/\delta P$, where ΔI was the relative current change, I_0 was the initial current of the M-SPF, and ΔP was the difference in pressure load). As shown in Fig. 5h, the prepared M-SPF sensor revealed a wide working pressure range from 0 to 800 kPa, corresponding to a strain range of 0–99.0%. As shown in Fig. 5i–k, we fit the curve of pressure and $\Delta I/I_0$, in which the slope of the linear equation represents the sensitivity.[50] The curves showed the highest sensitivity ($S1 = 63.4$ kPa^{-1}, $R^2 = 0.999$) in the low-pressure region (0–10 kPa) and exhibited a relatively lower sensitivity ($S2 = 48.5$ kPa^{-1}, $R^2 = 0.998$) in the medium-pressure region (10–100 kPa). Interestingly, the high-pressure region (>100 kPa) also displayed a high sensitivity of 22.6 kPa^{-1} (Fig. 5k), which should have been due to the large M-SPF deformation space. Furthermore, the relationship between current and force according to linear equations in different regions was also quantified. In comparison, the M-SPF sensitivity was superior to those reported for piezoresistive sensors, such as CNTs and rGO carbon frameworks.[51–53] Table S3† compares different materials.

Recently, several studies have reported the great influence of thickness on the sensitivity and conductivity of the piezoresistive sensor.[14,15,20,46] The fabricated M-SPF composite material was cut into different thicknesses of 2.0 mm, 3.0 mm, 4.0 mm and 5.0 mm for assembling pressure sensors. As shown in Fig. S10,† the current change rate gradually decreased with the increase of thickness under the same external force. The pressure sensitivity of the 5.0 mm thick M-SPF composite was

only 18 kPa^{-1}, and a high pressure sensitivity of 63.4 kPa^{-1} was obtained when decreased the thickness to 2.0 mm. The environmental stability is also an important criterion for evaluating the performance of pressure sensor.[14,20] As shown in Fig. S11,† the response of the same pressure sensor can still get a stable electrical signal output even after three months indicating the high stability of M-SPF.

In addition, the mechanical and sensing performance of the carbonized Shaddock peel powders (CSPP) and PDMS (CSPP–PDMS) compact composite was also measured for comparison. The preparation of CSPP–PDMS was based on previous literature with minor revise. The weight rate of CSPP and PDMS in CSPP–PDMS was consistent with the weight rate of C-SPF and PDMS for M-SPF. The SEM images showed that CSPP was uniformly dispersed in PDMS, and CSPP–PDMS displayed a non-porous dense surface (Fig. S12a†). The mechanical test showed that CSPP–PDMS had good compression-recovery performance when the strain was applied at 50.0%, but damaged after 10 cycles under 80.0% extreme strain (Fig. S12b and c†). Furthermore, the maximum RCR of the CSPP–PDMS sensor under 50.0% strain only 0.6% (Fig. S12d†), which is almost 3 orders of magnitude lower than M-SPF (Fig. 5c). Additionally, as a result of the high signal-to-noise ratio during compression-recovery cycles, it is almost impossible to accurately identify the small human physiological signals (such as pulses) with CSPP–PDMS sensor. These results indicated that the porous pressure sensing sensor based on C-SPF had a much better performance than the compact pressure sensing sensor based on CSPP.

3.4. M-SPF-based wearable sensor for body motion detection

Based on the excellent compressibility, stability, repeatability, high sensitivity, and timely pressure–current response performance discussed above, the prepared M-SPF sensor exhibited great potential as a lightweight and flexible wearable electronic device. A series of tests for detecting various human body movements were conducted (Fig. 7a) to prove its potential as a piezoresistive sensor. The assembled M-SPF sensor was attached to the human wrist, throat, foot, and face with the assistance of wound plastic to monitor human movement. Fig. 7b showed that the current could respond rapidly with a clear signal from a small force in the wrist pulse with the cyclicity of 66 beats per min. An amplified pulse pressure curve had two distinct peaks (the inset in Fig. 7b) corresponding with the systolic wave (P_1) and diastolic wave (P_2).[54] The transit time could be measured, which was defined as the time delay between the systolic peak and diastolic peak.[55,56] This increased with increasing degrees of finger bends, and the repetitive moving signals caused by elbow bending could also be identified clearly. As shown in Fig. 7g and h, the prepared sensor had different responsiveness to finger presses with different strengths under low and high frequencies. Furthermore, compared with the above movements, the prepared sensor displayed the strongest repetitive stable signal when stepped on by the foot (Fig. 7i). Therefore, M-SPF exhibited great promise for application in biosignal detection wearable devices.

4 Conclusions

Shaddock peel, a crop by-product, was developed as a flexible sensitive material for detecting environmental external pressure. The SP carbon-based porous framework (C-SPF) with a high conductivity was prepared using hydrothermal treatment followed by carbonization. Then, the PDMS elastomer was coated on the C-SPF framework instead of dense filling to convert the brittle C-SPF into porous elastic materials (M-SPF). Benefiting from the large deformation space of the porous framework and the stable interactions between PDMS and C-SPF, M-SPF exhibited excellent mechanical properties, even could resist an extreme compressive strain of 99.0% and maintain 99.4% height retention after 10 000 cycles at a strain of 50.0%. The as-prepared M-SPF-based piezoresistive sensor exhibited a fast response (loading and unloading stress in 20 ms and 30 ms), high sensitivity (63.4 kPa^{-1}), wide working range (from 0 to 800 kPa), and stable stress-current response (10 000 cycles). This breaks new ground for various applications, such as flexible wearable devices. The low cost, simple design and portable use of piezoresistive sensors highlight the potential application of SPs as high-value materials.

Conflicts of interest

There are no conflicts to declare.

Acknowledgements

This work was supported by the Opening Project of Guangxi Key Laboratory of Clean Pulp & Papermaking and Pollution Control (2019ZR05, ZR201805-7) and the Natural Science Foundation of Guangxi (2018JJA130224).

References

1 W. Gao, S. Emaminejad, H. Y. Y. Nyein, S. Challa, K. Chen, A. Peck, H. M. Fahad, H. Ota, H. Shiraki, D. Kiriya, D. H. Lien, G. A. Brooks, R. W. Davis and A. Javey, *Nature*, 2016, **529**, 509–514.
2 G. Schwartz, B. C. Tee, J. Mei, A. L. Appleton, D. H. Kim, H. Wang and Z. Bao, *Nat. Commun.*, 2013, **4**, 1859.
3 L. Han, J. Ding, S. Wang, J. Xu, N. Yuan, G. Cheng and Z. Liu, *Sci. China: Technol. Sci.*, 2018, **61**, 1137–1143.
4 Z. Wang, S. Wang, J. Zeng, X. Ren, A. J. Chee, B. Y. Yiu, W. C. Chung, Y. Yang, A. C. Yu, R. C. Roberts, A. C. Tsang, K. W. Chow and P. K. Chan, *Small*, 2016, **12**, 3827–3836.
5 X. Wang, Y. Gu, Z. Xiong, Z. Cui and T. Zhang, *Adv. Mater.*, 2014, **26**, 1336–1342.
6 J. Park, M. Kim, I. Hong, T. Kim, E. Lee, E. A. Kim, J. K. Ryu, Y. Jo, J. Koo, S. Han, J. S. Koh and D. Kang, *Sensors*, 2019, **19**, 5504.
7 L. Q. Tao, K. N. Zhang, H. Tian, Y. Liu, D. Y. Wang, Y. Q. Chen, Y. Yang and T. L. Ren, *ACS Nano*, 2017, **11**, 8790–8795.
8 Z. Chen, Z. Wang, X. Li, Y. Lin, N. Luo, M. Long, N. Zhao and J. B. Xu, *ACS Nano*, 2017, **11**, 4507–4513.

9 D. Kwon, T. I. Lee, J. Shim, S. Ryu, M. S. Kim, S. Kim, T. S. Kim and I. Park, *ACS Appl. Mater. Interfaces*, 2016, **8**, 16922–16931.
10 K. Parida, V. Bhavanasi, V. Kumar, R. Bendi and P. S. Lee, *Nano Res.*, 2017, **10**, 3557–3570.
11 H. Zhang, N. Liu, Y. Shi, W. Liu, Y. Yue, S. Wang, Y. Ma, L. Wen, L. Li, F. Long, Z. Zou and Y. Gao, *ACS Appl. Mater. Interfaces*, 2016, **8**, 22374–22381.
12 H. P. Phan, T. Dinh, T. Kozeki, T.-K. Nguyen, A. Qamar, T. Namazu, N.-T. Nguyen and D. V. Dao, *IEEE Electron Device Lett.*, 2016, **37**, 1029–1032.
13 Y. Wang, M. Chao, P. Wan and L. Zhang, *Nano Energy*, 2020, **70**, 104560.
14 P. M. Pataniya, C. K. Sumesh, M. Tannarana, C. K. Zankat, G. K. Solanki, K. D. Patel and V. M. Pathak, *Nanotechnology*, 2020, **31**, 435503.
15 P. M. Pataniya, S. A. Bhakhar, M. Tannarana, C. Zankat, V. Patel, G. K. Solanki, K. D. Patel, P. K. Jha, D. J. Late and C. K. Sumesh, *J. Colloid Interface Sci.*, 2021, **584**, 495–504.
16 Z. Zhang, Y. Zhang, X. Jiang, H. Bukhari, Z. Zhang, W. Han and E. Xie, *Carbon*, 2019, **155**, 71–76.
17 Z. Yue, Y. Zhu, J. Xia, Y. Wang, X. Ye, H. Jiang, H. Jia, Y. Lin and C. Jia, *ACS Appl. Electron. Mater.*, 2021, **3**, 1301–1310.
18 Z. Liu, K. Wan, T. Zhu, J. Zhu, J. Xu, C. Zhang and T. Liu, *ACS Appl. Mater. Interfaces*, 2021, **13**, 7580–7591.
19 G. Ge, Y. Cai, Q. Dong, Y. Zhang, J. Shao, W. Huang and X. Dong, *Nanoscale*, 2018, **10**, 10033–10040.
20 D. Kannichankandy, P. M. Pataniya, S. Narayan, V. Patel, C. K. Sumesh, K. D. Patel, G. K. Solanki and V. M. Pathak, *Synth. Met.*, 2021, **273**, 116697.
21 X. Lin, T. Zhang, J. Cao, H. Wen, T. Fei, S. Liu, R. Wang, H. Ren and H. Zhao, *J. Bionic. Eng.*, 2020, **17**, 55–63.
22 X. Zang, Y. Jiang, X. Wang, X. Wang, J. Ji and M. Xue, *Sens. Actuators, B*, 2018, **273**, 1195–1201.
23 Y. Ding, T. Xu, O. Onyilagha, H. Fong and Z. Zhu, *ACS Appl. Mater. Interfaces*, 2019, **11**, 6685–6704.
24 Y. Huang, Y. Chen, X. Fan, N. Luo, S. Zhou, S. C. Chen, N. Zhao and C. P. Wong, *Small*, 2018, **14**, 1801520.
25 J. Huang, M. Zhao, Y. Cai, M. Zimniewska, D. Li and Q. Wei, *Adv. Electron. Mater.*, 2019, **6**, 1900934.
26 B. Wang, T. Shi, Y. Zhang, C. Chen, Q. Li and Y. Fan, *J. Mater. Chem. C*, 2018, **6**, 6423–6428.
27 J. Huang, D. Li, M. Zhao, H. Ke, A. Mensah, P. Lv, X. Tian and Q. Wei, *Chem. Eng. J.*, 2019, **373**, 1357–1366.
28 R. Huang, M. Cao, H. Guo, W. Qi, R. Su and Z. He, *J. Agric. Food Chem.*, 2014, **62**, 4643–4651.
29 J. Li, W. Liu, D. Xiao and X. Wang, *Appl. Surf. Sci.*, 2017, **416**, 918–924.
30 C. Zhao, P. Lv, L. Yang, S. Xing, W. Luo and Z. Wang, *Energy Convers. Manage.*, 2018, **160**, 477–485.
31 M. E. Argun, D. Güclü and M. Karatas, *J. Ind. Eng. Chem.*, 2014, **20**, 1079–1084.
32 A. Yin, F. Xu and X. Zhang, *Materials*, 2016, **9**, 758.
33 N. Luo, Y. Huang, J. Liu, S. C. Chen, C. P. Wong and N. Zhao, *Adv. Mater.*, 2017, **29**, 1702675.
34 Q. J. L. F. Wanga, T. E. Glassb, T. C. Wardb, J. E. McGrathb, M. Mugglic, G. Burnsd and U. Sorathiae, *Polymer*, 2000, **41**, 5083–5093.
35 J. N. Chazalviel and U. P. Rodrigues-Filho, *Thin Solid Films*, 2012, **520**, 3918–3921.
36 X. Zhao, L. X. Li, B. C. Li, J. P. Zhang and A. Q. Wang, *J. Mater. Chem. A*, 2014, **2**, 18281–18287.
37 Z. Chen, H. Zhuo, Y. Hu, H. Lai, L. Liu, L. Zhong and X. Peng, *Adv. Funct. Mater.*, 2020, **30**, 1910292.
38 K. Zhou, C. Chen, M. Lei, Q. Gao, S. Nie, X. Liu and S. Wang, *RSC Adv.*, 2020, **10**, 2150–2159.
39 Q. Luo, H. Zheng, Y. Hu, H. Zhuo, Z. Chen, X. Peng and L. Zhong, *Ind. Eng. Chem. Res.*, 2019, **58**, 17768–17775.
40 P. Ieamviteevanich, D. Palaporn, N. Chanlek, Y. Poo-arporn, W. Mongkolthanaruk, S. J. Eichhorn and S. Pinitsoontorn, *ACS Appl. Nano Mater.*, 2020, **3**, 3939–3950.
41 L. Qiu, J. Z. Liu, S. L. Chang, Y. Wu and D. Li, *Nat. Commun.*, 2012, **3**, 1241.
42 S. Zhang, K. Sun, H. Liu, X. Chen, Y. Zheng, X. Shi, D. Zhang, L. Mi, C. Liu and C. Shen, *Chem. Eng. J.*, 2020, **387**, 124045.
43 Y. Qin, Y. Ding, Z. Lin, C. Wang, Y. Li, F. Xu, J. Li, Y. Yuan, X. He and Y. Li, *ACS Nano*, 2015, **9**, 8933–8941.
44 Y. Huang, Y. Chen, X. Fan, N. Luo, S. Zhou, S. Chen, N. Zhao and C. Wong, *Small*, 2018, **14**, 1801520.
45 Y. Ding, J. Yang, C. R. Tolle and Z. Zhu, *ACS Appl. Mater. Interfaces*, 2018, **10**, 16077–16086.
46 Y. Li, Y. A. Samad and K. Liao, *J. Mater. Chem. A*, 2015, **3**, 2181–2187.
47 B. Zhang, Z. Hou, W. Yan, Q. Zhao and K. Zhan, *Carbon*, 2017, **125**, 199–206.
48 Y. Wei, S. Chen, X. C. Dong, Y. Lin and L. Liu, *Carbon*, 2017, **113**, 395–403.
49 M. N. Tsui and M. F. Islam, *Nanoscale*, 2017, **9**, 1128–1135.
50 X. Liao, Q. Liao, X. Yan, Q. Liang, H. Si, M. Li, H. Wu, S. Cao and Y. Zhang, *Adv. Funct. Mater.*, 2015, **25**, 2395–2401.
51 J. Yang, Y. Ye, X. Li, X. Lu and R. Chen, *Compos. Sci. Technol.*, 2018, **164**, 187–194.
52 X. Wu, X. Liu, J. Wang, J. Huang and S. Yang, *ACS Appl. Mater. Interfaces*, 2018, **10**, 39009–39017.
53 F. A. Khan, C. M. Ajmal, S. Bae, S. Seo, H. Moon and S. Baik, *Small*, 2018, **14**, 1800549.
54 X. Wu, Y. Han, X. Zhang, Z. Zhou and C. Lu, *Adv. Funct. Mater.*, 2016, **26**, 6246–6256.
55 C. L. Choong, M. B. Shim, B. S. Lee, S. Jeon, D. S. Ko, T. H. Kang, J. Bae, S. H. Lee, K. E. Byun, J. Im, Y. J. Jeong, C. E. Park, J. J. Park and U. I. Chung, *Adv. Mater.*, 2014, **26**, 3451–3458.
56 E. Chung, G. Chen, B. Alexander and M. Cannesson, *Front. Med.*, 2013, **7**, 91–101.
57 H. Zhuo, Y. Hu, X. Tong, Z. Chen, L. Zhong, H. Lai, L. Liu, S. Jing, Q. Liu, C. Liu, X. Peng and R. Sun, *Adv. Mater.*, 2018, **30**, 1706705.
58 H. Sun, Z. Xu and C. Gao, *Adv. Mater.*, 2013, **25**, 2554–2560.
59 X. Wang, L. L. Lu, Z. L. Yu, X. W. Xu, Y. R. Zheng and S. H. Yu, *Angew. Chem., Int. Ed. Engl.*, 2015, **54**, 2397–2401.
60 L. Li, B. Li, H. Sun and J. Zhang, *J. Mater. Chem. A*, 2017, **5**, 14858–14864.
61 J. P. Zhang, B. C. Li, L. X. Li and A. Q. Wang, *J. Mater. Chem. A*, 2016, **4**, 2069–2074.

62 Y. Si, X. Wang, C. Yan, L. Yang, J. Yu and B. Ding, *Adv. Mater.*, 2016, **28**, 9512.
63 Y. Hu, H. Zhuo, Q. Luo, Y. Wu, R. Wen, Z. Chen, L. Liu, L. Zhong, X. Peng and R. Sun, *J. Mater. Chem. A*, 2019, **7**, 10273–10281.
64 X. Peng, K. Wu, Y. Hu, H. Zhuo, Z. Chen, S. Jing, Q. Liu, C. Liu and L. Zhong, *J. Mater. Chem. A*, 2018, **6**, 23550–23559.
65 M. Yang, N. Zhao, Y. Cui, W. Gao, Q. Zhao, C. Gao, H. Bai and T. Xie, *ACS Nano*, 2017, **11**, 6817–6824.
66 J. Liu, Y. Liu, H. B. Zhang, Y. Dai, Z. Liu and Z. Z. Yu, *Carbon*, 2018, **132**, 95–103.
67 M. Kotal, H. Kim, S. Roy and I. K. Oh, *J. Mater. Chem. A*, 2017, **5**, 17253–17266.
68 Y. Li, J. Chen, L. Huang, C. Li, J. D. Hong and G. Shi, *Adv. Mater.*, 2014, **26**, 4789–4793.
69 H. L. Gao, Y. B. Zhu, L. B. Mao, F. C. Wang, X. S. Luo, Y. Y. Liu, Y. Lu, Z. Pan, J. Ge, W. Shen, Y. R. Zheng, L. Xu, L. J. Wang, W. H. Xu, H. A. Wu and S. H. Yu, *Nat. Commun.*, 2016, **7**, 12920.
70 C. Chen, J. Song, S. Zhu, Y. Li, Y. Kuang, J. Wan, D. Kirsch, L. Xu, Y. Wang, T. Gao, Y. Wang, H. Huang, W. Gan, A. Gong, T. Li, J. Xie and L. Hu, *Chem*, 2018, **4**, 544–554.
71 S. Barg, F. M. Perez, N. Ni, P. do Vale Pereira, R. C. Maher, E. Garcia-Tunon, S. Eslava, S. Agnoli, C. Mattevi and E. Saiz, *Nat. Commun.*, 2014, **5**, 4328.
72 H. Zhuo, Y. Hu, Z. Chen, X. Peng, H. Lai, L. Liu, Q. Liu, C. Liu and L. Zhong, *ACS Sustainable Chem. Eng.*, 2020, **8**, 11921–11929.